Aqueous Diffusion Pathways as a Part of the Ventricular Cell Ultrastructure

A. S. Parfenov, V. Salnikov, W. J. Lederer, and V. Lukyánenko
Medical Biotechnology Center, University of Maryland Biotechnology Institute, Baltimore, Maryland

ABSTRACT The physical organization of the ventricular myocyte includes barriers for the movement of objects of varying dimensions ranging from ions to solid particles. There are two kinds of diffusion in the cell: lateral (in membranes) and aqueous. Here we examine the size constraints of aqueous diffusion pathways and discuss their impact on cellular physiology. Calibrated gold nanoparticles were used to probe the accessibility of the entire transverse-axial tubular system (TATS), the sarcoplasm, and intracellular structures. The TATS tubules, although up to 300 nm in diameter, permitted only particles $\leq$11 nm to enter. When calibrated nanoparticles were added to permeabilized ventricular cells, particles $\leq$11 nm were found in the sarcoplasm. The distribution of nanoparticles in the cells allowed us to conclude that 1), the TATS and the sarcoplasm are accessible only for particles $\leq$11 nm; 2), the gaps between T-tubules and junctional sarcoplasmic reticulum (jSR), jSR and mitochondria, and intermitochondrial contacts are inaccessible for particles with physical size $>$3 nm; 3), the mitochondrial voltage-dependent anion channel and the nuclear pore complex in ventricular cells could not be penetrated by particles $\geq$6 nm; and 4), there is a difference in size clearance between transversal and longitudinal sarcoplasmic diffusional pathways.

INTRODUCTION

Heart physiology is very dependent on aqueous diffusion of ions and macromolecules in the sarcoplasm. The structure of a ventricular cell supposes the existence of diffusion pathways between myofibrils and around mitochondria. The ultrastructure of a ventricular cell (Fig. 1) shows the existence of intracellular spaces where the free sarcoplasmic diffusion of macromolecules, such as structural and/or regulatory proteins (1–4), could be significantly restricted. There are at least four such regions inside the ventricular cell. They are 1), the space between the junctional sarcoplasmic reticulum (jSR) and the transverse-axial tubular system (TATS), also known as the junctional cleft (JC); 2), the intermitochondrial junctions, which putatively allow mitochondria to synchronize their physiology; 3), the mitochondrial intermembrane space; and 4), the nucleus.

The structural organization of the space around the jSR is a matter of special interest because of its direct involvement in excitation-contraction coupling. This space includes a region between the intermyofibrillar mitochondrion (IMFM) and the transverse tubule of TATS (T-tubule). Electron micrographs (5–7; and our data presented in Fig. 1) show how tightly the intracellular microstructures are packed in this peri-jSR region. The sarcoplasmic diffusion of big proteins could be restricted to the JC by physical contact between ryanodine receptors, and to the cleft between IMFM and the jSR by connecting pillars (Fig. 1 *C*) from the sarcoplasm and voltage-dependent anion channels (VDACs) from the IMFM intermembrane space. Thus, knowing the physical size of diffusion paths for the structural and regulatory proteins in a cardiac cell is crucial for understanding physiological processes on the cellular level.

Electron microscopy (EM) is currently the only existing technique for measuring nanometer intracellular distances. However, structural distortions resulting from the fixation of tissue for EM make measurements from micrographs less valuable. These distortions result from fixation of muscle tissue, staining, dehydration, and embedding (total shrinkage in volume can be ~50% (8)). Additionally, protein configurations were recognized as being severely damaged with OsO_4 (9). These distortions can seriously influence the final picture and corresponding intracellular measurements. Moreover, as a result of the distortions, the diffusional pathways should change much more than intracellular structures because they are relatively ''empty'' and could be significantly reduced during the myocyte shrinkage.

Currently, the existence of only one ''intracellular'' system of aqueous diffusion pathways has been reported: the TATS (10–12). Although located inside the ventricular cell, TATS is not a true intracellular system because of its multiple contacts with the extracellular space through T-tubules. Usually the diameters of the T-tubules fall within the range of ~200–360 nm (10,12). The tubules are filled with glycocalyx. The glycocalyx interconnects with ''fibrillar bodies'' and that creates a mesh inside them (1,6,10). As it is formally a sarcolemma invagination, TATS helps to spread the action

---

Submitted August 1, 2005, and accepted for publication October 21, 2005.

Address reprint requests to Dr. Valériy Lukyánenko, Medical Biotechnology Center, University of Maryland Biotechnology Institute, 725 W. Lombard St., Rm. S216, Baltimore, MD 21201. Tel.: 410-706-8559; Fax: 410-706-8184; E-mail: lukyanen@umbi.umd.edu.

Dr. Parfenov's permanent address is General Physics Institute, Russian Academy of Sciences, 38 L-2 Vavilov St., Moscow, Russia 119992.

Dr. Salnikov's permanent address is Kazan Institute of Biochemistry and Biophysics, Kazan Science Center, Russian Academy of Sciences, 2/31 Lobachevskii St., Kazan, Russia 420111.

0006-3495/06/02/1107/13 $2.00

doi: 10.1529/biophysj.105.071787

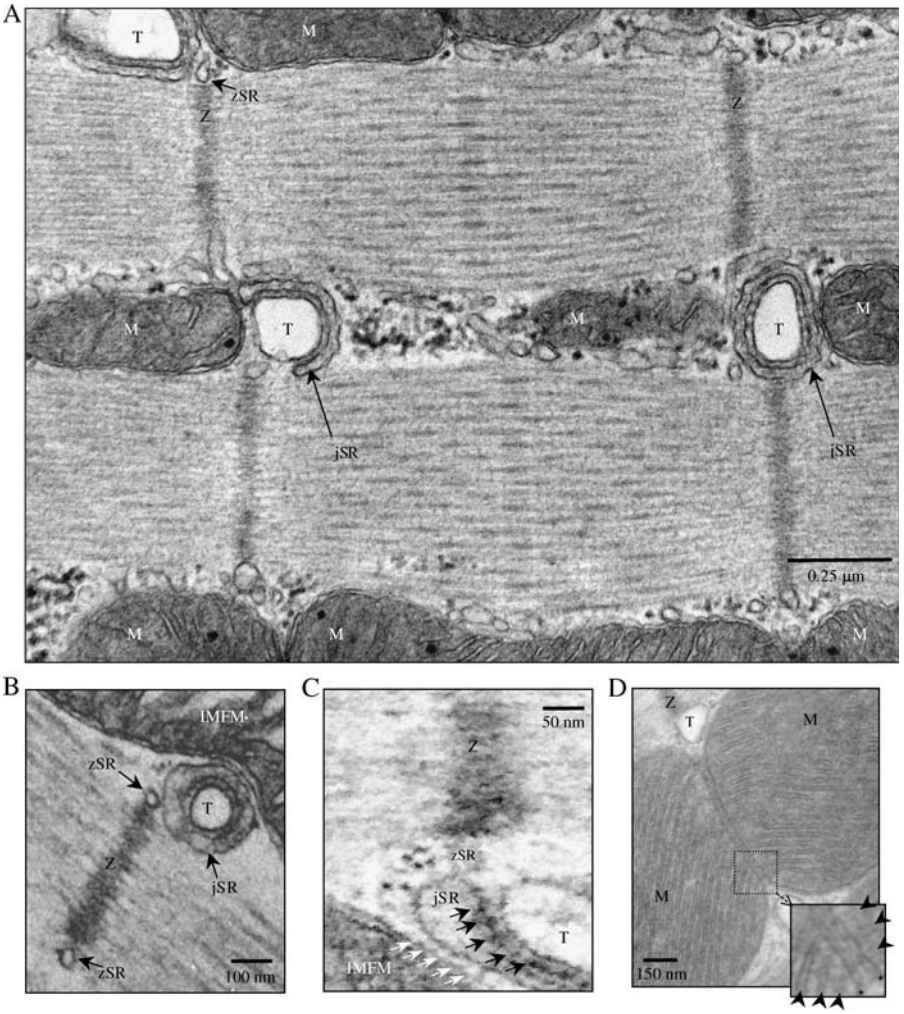

FIGURE 1 Spatially restricted zones inside a ventricular cell. (*A–D*) The electron micrographs (longitudinal ultrathin section, Epon embedding) visualize ventricular cell ultrastructure after fixation and resin polymerization. Areas between mitochondria, between a mitochondrion and jSR, and between jSR and T-tubules look like structurally restricted zones for the diffusion of big cytoplasmic molecules. *T*, T-tubules; *jSR*, junctional SR; *zSR*, z-tubules of the SR; *M*, mitochondrion; *Z*, Z line; *IMFM*, intermyofibrillar mitochondrion, *solid arrows*, feet (RyRs). Open arrows show structures connecting the IMFM and jSR. (*D*) Intermitochondrial contact. Inset shows the ultrastructural organization of the contact. Arrowheads show mitochondrial cristae; asterisks show double mitochondrial membranes.

potential and provides for diffusive access for ions, hormones, and metabolic substrates throughout the thickness of the cardiac cell. The T-tubule sarcolemma contains numerous transporting structures and receptors crucial for cardiac function.

In this article, we report for the first time what we know about the real accessibility of TATS and sarcoplasmic aqueous diffusion pathways.

METHODS

To probe the physical size of TATS tubules and sarcoplasmic aqueous diffusion pathways in vivo, we loaded isolated intact or saponin-permeabilized ventricular myocytes with calibrated nanogold particles before fixation for EM. The diameter of the particles used corresponded approximately to the size of the smallest and biggest cellular aqueous pathways. For example, the diameter of hydrated Ca^{2+}, which is the major cation involved in excitation-contraction coupling, is ~0.6 nm (ionic radius, ~0.12 nm, plus the width of the hydration shell, 0.17 nm, from seven water molecules (13)). Taking into account the number of other sarcoplasmic ions and molecules, Ca^{2+} could diffuse relatively freely through aqueous pathways with diameters of ~2–3 nm. Gold sols of this size are commercially available (Ted Pella, Redding, CA) but must be stabilized to prevent their aggregation in salt solutions (14).

The maximal size of the nanoparticles to be used for this research was related to the physical size of intracellular proteins, extracellular hormones, and the minimal size of the T-tubules (see above). Proteins with molecular mass of 62–156 kDa were shown to have a radius of gyration of 3.4–7.2 nm (15). Uncharged hormones that are effective for ventricular cells (1) must be similar in size to nonelectrolytes, and their hydrodynamic radii should be between 0.6 and 2.1 nm for a molecular mass range of 0.2–4.6 kDa (16). Thus, we used commercially available gold nanoparticles ranging in size from 2 to 50 nm. The aggregation of the particles in experimental solution and their binding to proteins (17) was prevented by stabilizing (coating) them with polyvinylpyrrolidone (PPV) (18,19). This was shown to allow free diffusion of the particles in the cytoplasm (18) and was used for measurements of the physical size of the nuclear pore under different experimental conditions in oocytes and fibroblasts (18,20–22).

Cell isolation and experimental solutions

Single ventricular myocytes were obtained from adult male Sprague-Dawley rat hearts by enzymatic dissociation as described previously (23). The animals were killed by lethal intraperitoneal injection of Nembutal (100 mg/kg). The standard Tyrode solution contained (in mM): 140 NaCl, 5.4 KCl, 0.5 $MgCl_2$, 1 $CaCl_2$, 10 Hepes, 0.25 NaH_2PO_4, and 5.6 glucose, pH 7.3. Unless specified otherwise, all chemicals were from Sigma (St. Louis, MO). To overload the sarcoplasmic reticulum (SR) of ventricular cells with Ca^{2+}

and induce spontaneous contraction of ventricular cells, $[Ca^{2+}]$ in Tyrode solution was increased to 5 mM (24).

Isolated ventricular cells were permeabilized by exposure to 0.01% saponin for 1 min. The permeabilization solution contained 100 mM K^+ aspartate, 20 mM KCl, 3 mM MgATP, 0.81 $MgCl_2$ ($[Mg^{2+}]_{free} = \sim 1$ mM), 0.5 mM EGTA, 0.114 $CaCl_2$ ($[Ca^{2+}]_{free} = \sim 100$ nM), 20 mM Hepes, 3 mM glutamic acid, and 3 mM malic acid, pH 7.2. The control experimental solution for permeabilized cells contained: 100 mM K aspartate, 20 mM KCl, 3 mM MgATP, 0.81 $MgCl_2$ ($[Mg^{2+}]_{free} = \sim 1$ mM), 0.1 mM EGTA, 0.03 $CaCl_2$ ($[Ca^{2+}]_{free} = \sim 60$ nM), 20 mM Hepes, 10 mM phosphocreatine, 5 U/ml creatine phosphokinase, 3 mM glutamic acid, and 3 mM malic acid, pH 7.2. The free $[Ca^{2+}]_{free}$ and $[Mg^{2+}]_{free}$ at the given total Ca^{2+}, Mg^{2+}, ATP, and EGTA concentrations were calculated using WinMAXC 2.4 (Stanford University, Stanford, CA). $[Ca^{2+}]_{free}$ was confirmed by measurements with a spectrofluorometer D-Scan (PTI, Monmouth Junction, NJ) and the Ca^{2+} indicator fura-2 (TefLabs, Austin, TX).

Electron microscopic studies

Rat isolated ventricular cells were fixed in 6% glutaraldehyde in 0.1 M Na-cacodylate buffer (pH 7.4), for 20 min at room temperature, then rinsed two times with the same buffer supplemented with 0.1 M sucrose and postfixed with 1% osmium in Na-cacodylate buffer. Then samples were en block stained (1% uranyl acetate in 25% ethanol) for 1 h. After dehydration in an alcohol series, the samples were embedded in LR White resin (Ted Pella, Redding, CA). Ultrathin sections were obtained with an LKB III microtome (LKB, Uppsala, Sweden), collected on formvar-coated nickel grids, and stained for 15 min with 2% aqueous uranyl acetate and then for 2 min with lead citrate at room temperature. Sections were examined at 60 kV with a Zeiss electron microscope EM 10C/EM 10 CR (Zeiss, Göttingen, Germany). Images were stored in tif format.

Silver enhancement for gold nanoparticles was made with the BBInternational Silver Enhancing Kit (Ted Pella). The size of the silver grains depends on the time of exposure and the accessibility (i.e., depth of position within the section) of the gold. We applied the solution for 8 min. To reveal highly electron-dense silver particles, we digitally reduced image contrast by 70–80% with Adobe Photoshop 7.0 (Adobe Systems, San Jose, CA). Small silver grains that cannot be seen clearly on the presented micrographs under the given resolution were marked with blue ovals. Note that although they preserved cell content and structures, fast fixation and silver enhancement reduced the quality of the EM images, making invisible some delicate intracellular membrane structures (Golgi apparatus, vesicles, etc.).

Representative micrographs (see Figs. 4–9) show the typical distribution of nanoparticles for 100–200 cells. ImageJ 1.31v (National Institutes of Health, Bethesda, MD) was used to calculate the number of particles in 10-μm^2 regions within the outer cell borders, including all cell organelles except for the nucleus.

Data were expressed as particles/μm^3, taking into account that we visualized particles in the entire thickness of an ultrathin section and assuming the average thickness of the section to be 80 nm. Data were expressed as mean ± SE. Comparisons were performed by using the Student's *t*-test, and differences were considered significant when $P < 0.05$.

Recording of reflected light

To visualize gold particles in the experimental solution, we illuminated them with an argon (488 nm) laser beam. The reflected light was recorded with a Carl Zeiss Laser Scanning Confocal System (LSM 510, Carl Zeiss, Oberkochen, Germany) equipped with a C-Apochromat 63×/1.2 W corr objective using the emission filter LP475 (i.e., 475 nm). All measurements were made from optical slices <1 μm thick. To prevent the effect of possible heating of nanogold particles, we maximally restricted the number of laser scans and the laser beam power (~0.08 mW).

Probing of prefixed intracellular distances with nanoparticles

To measure prefixational distances between intracellular structures, we used calibrated colloidal gold sols (from 2 to 50 nm; Ted Pella) stabilized with 1% PVP. Permeabilized cells were incubated with gold nanoparticles for 20 min as has been done by others (22). Traces of sodium citrate in colloidal gold (0.01%) probably reduced $[Mg^{2+}]_{free}$ significantly in the experimental solution. The decreased concentration of this ryanodine receptor (RyR, the SR Ca^{2+} channel) inhibitor (25) in the intracellular solution resulted in spontaneous Ca^{2+} waves (24). For experiments with quiescent permeabilized cells, this decrease in $[Mg^{2+}]$ was compensated with an additional 0.25 mM $MgCl_2$. The permeabilization of the cells before fixation for EM was confirmed with confocal microscopy and a membrane-impermeant potassium salt of fluo-3 (Biotium, Hayward, CA), as was shown earlier (26).

To measure the size of the PVP-coated nanoparticles, we employed dynamic light scattering (DynaPro, Wyatt Technology, Santa Barbara, CA). These measurements showed that 1% PVP increased the diameter of the gold particles, adding ~2 nm to their original size. We assumed that after fixation for EM these nanoparticles would be found trapped in areas with dimensions similar to theirs. Larger particles would not be found in some areas because they could not enter them, and smaller particles would be washed out during fixation for EM. Thus, in this case the particle size should correspond to the size of the region in vivo, i.e., before fixation. Although we know the average size of the particles in a group, theoretically the smallest particles must penetrate deeper into the cell and will be found in bigger numbers than particles with average size. Taking into account the divergence in size (17) and shape (the PVP-coated particles are not perfectly spherical (19,27)) within a group, the smallest PVP-coated particles in a group should be ~1 nm smaller than the average size. Thus, in our experiments we used groups of particles with minimal sizes of ~3, 6, 11, 16, 21, 28, 51, and 96 nm.

To verify the stabilizing effect of PVP, we used EM and spectroscopy (Fig. 2). Dried 10-nm colloidal gold particles (from water suspension) are seen on an EM micrograph (no silver enhancement or contrasting) as separated particles (Fig. 2 *A*). The addition of a major compound of our experimental solution, potassium aspartate (150 mM, pH 7.2; Fig. 2, *blue line*), resulted in predictable (14) aggregation of particles (Fig. 2 *B*). This aggregation was successfully prevented with PVP coating (Fig. 2 *C*). We confirmed the data using a spectrophotometer (Cary 300 Bio; Varian, Walnut Creek, CA). As gold nanoparticles have a strong surface-plasmon band absorbance in the visible spectrum (maximum at ~523 nm), particle aggregation can be measured as either the broadening of the peak or as a red peak shift in the absorbance spectra (14,28). In agreement with this, 10 nm colloidal gold in our experiments demonstrated maximum absorbance at 520 nm (Fig. 2 *D*, *black line*; $n = 8$), and the addition of 150 mM potassium aspartate (pH 7.2) shifted the peak to ~620 nm (Fig. 2 *D*, *blue line*). Coating of the gold nanoparticles with PVP did not cause this shift (Fig. 2 *D*, *red line*; absorbance maximum at 521 nm) and prevented the aggregation of the particles with potassium aspartate (Fig. 2 *D*, *green line*). Moreover, PVP also prevented the attachment of coated particles to proteins (Fig. 2 *E*), which were represented by bovine serum albumin (14).

The 50-nm colloidal gold in our experiments demonstrated an absorbance maximum at 532.7 ± 0.4 nm ($n = 7$). The comparison of effects from different concentrations of PVP on the absorbance maximum showed an insignificant difference for 0.3% and 5% PVP coating both for 10-nm (521 ± 0.2 nm and 521 ± 0.6 nm, respectively; $n = 4$ each) and 50-nm (533 ± 0.3 nm and 533 ± 0.1 nm, respectively; $n = 4$ each) particles. All compounds used in our experimental solutions and laminin were investigated in the used concentrations for induction of aggregation of 10-nm gold particles stabilized in 1% PVP. Neither one of them shifted the absorbance maximum for colloidal gold.

Because polymer-coated gold particles were shown to move in the cytoplasm at a velocity of ~0.5 μm/s (for 40-nm gold particles coated with polyethylene glycol delivered by injection (29)), we added nanoparticles to quiescent or spontaneously contracting intact or saponin-permeabilized

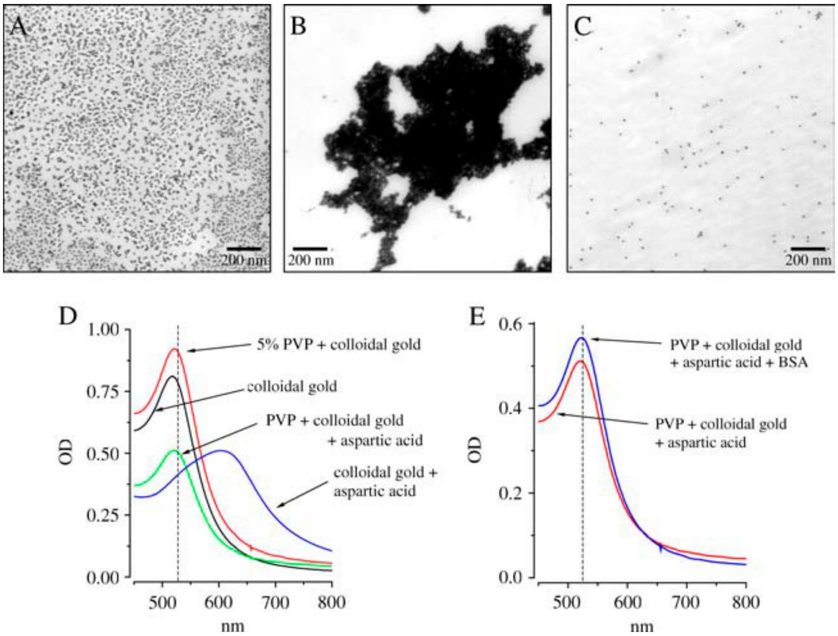

FIGURE 2 Stabilizing effect of PVP on gold nanoparticles. (*A–C*) Electron micrographs (without silver enhancement) show 10-nm sols (*A*) in water, (*B*) in 150 mM potassium aspartate solution, pH 7.2, and (*C*) pretreated with 1% PVP in aspartic acid solution. The suspensions were air-dried on formvar-coated grids, with no staining. (*D*) The absorption spectra for colloidal gold (*black line*, peak at 520 nm) and mixtures of gold and 150 mM potassium aspartate (*blue line*, pH 7.2), 5% PVP (*red line*), or 5% PVP and 150 mM potassium aspartate (*green line*, pH 7.2). Optical density (*OD*) depends on gold particle concentration; dashed lines show the absorbance maximum for colloidal gold (523 nm). (*E*) The absorption spectra for 10-nm colloidal gold stabilized with 5% PVP before (*red line*) and after (*blue line*) adding 1% bovine serum albumin to the cuvette.

ventricular cells 20 min before fixation for electron microscopy. Before application, the particles were pretreated for 10 min in 1% PVP (neutral; 10,000 mol wt) and supplemented with concentrated (10-fold) experimental solution. This reduced the density of the particles by ~20% from the original (2 nm, 1.5×10^{14} particles/ml; 5 nm, 5×10^{13} particles/ml; 10 nm, 5.7×10^{12} particles/ml; etc., Ted Pella).

Experiments were performed at room temperature (21–23°C).

RESULTS

To study the physical diameters of the diffusion pathways with nanoparticles, we used two approaches: confocal microscopy and EM. Confocal microscopy allows the recording of light reflection from the nanoparticles in vivo from an optical slice <1 μm thick. Unfortunately, our experiments showed that this approach could be valuable only with particles ≥50 nm. Thus, the majority of the experiments were performed using EM and silver enhancement. Although the latter allowed nanoparticles of any size to be visualized with EM, preparation for EM changes intracellular distances and structures, as mentioned above. To estimate the input of fixation and embedding, we used confocal microscopy to measure cell dimensions from the same group of six permeabilized cells before fixation, during fixation, and in the early stages of embedding, and EM to make measurements after resin polymerization. Similar to experiments performed earlier in intact single skeletal frog muscle fibers (8) our experiment showed a significant decrease in all cell dimensions (Table 1). In contrast to intact skeletal muscle fibers, the changes of volume in permeabilized cardiac cells do not depend on osmotic processes. They were negative through all stages of fixation and embedding, and before resin polymerization the average cell volume was reduced by ~15%. Resin polymerization resulted in a further reduction in the cell size. The average distance between Z-lines was reduced by 20% in comparison to the original. However, the distance between Z-lines in EM depends on the cutting angle, and only minimal size is really important. The minimal value for an EM sarcomere was 1.1 μm in our measurements.

TABLE 1 Average cell dimensions during the preparation of permeabilized ventricular cell for electron microscopy

	Length (μm)				
Stage of preparation for EM	Cell	Sarcomere	Width (μm)	Thickness (μm)	Volume (10^3 μm^3)
Before fixation	90.3 ± 3.6	1.87 ± 0.04	28.7 ± 1.6	14.3 ± 1.2	37.3 ± 3.9
Before polymerization	84.1 ± 3.6	—	26.7 ± 1.5	14.2 ± 1.2	31.7 ± 3.1
After polymerization	—	1.48 ± 0.06	—	—	20.1*–27.1
Difference (%)	−6.9	−20.9	−7.0	−1.1	−27* or −46*
P	<0.01	<0.00001	<0.05	0.611	<0.001

3D confocal (before and after fixation) and electron (after resin polymerization) microscopy. The data presented are for the same six cells, except in the case of sarcomere measurements, where *n* was 15 for measurements before fixation (control) and 10 for measurements after polymerization. *P* is derived from paired *t*-tests except measurements of sarcomeres.

*Values were derived from minimal size (1.1 μm) of sarcomere after resin polymerization assuming no changes in cell thickness and width.

This shows a reduction in sarcomere length after resin polymerization of ~37%. Even assuming no changes in cell thickness and width during the polymerization, cell volume after preparation for EM was reduced by ~46% in comparison to the original. These changes in volume are consistent with those reported earlier for skeletal muscle fibers (8).

Our measurements of sarcomeres in EM micrographs did not reveal a difference between intact and permeabilized ventricular cells embedded in LR White resin (1.50 ± 0.02 μm and 1.49 ± 0.02 μm, and $n = 58$ and 76, respectively; minimal values are ~1.1 μm). The embedding of the ventricular cells in Epon resin reduced the sarcomeres to a similar size (1.45 ± 0.03 μm; from 32 micrographs; minimal values are ~1.1 μm). This shows that the changes in sarcomere size do not depend on permeabilization or the embedding method for EM.

Intact ventricular cells

For confocal microscopy we increased the density of the 51-nm particles by ~10 times with passive precipitation. The experiments showed that TATS and the sarcoplasm are definitely not available for particles bigger then 50 nm. The 51-nm particles could enter neither the TATS of intact ventricular myocytes ($n = 20$) nor the sarcoplasm of permeabilized cells ($n = 20$). Fig. 3 *A* shows an intact cell (located inside the marked area) just 5 min after 51 nm particles were added to the bathing solution. The 51-nm particles are seen as the brightest dots in the experimental solution and along the sarcolemma contouring the cell. Digital contrast allows us to see that the particles are localized only outside the cell. The bright structures on the two ends of the nucleus are unidentified cell ultrastructures. Fig. 3 *B* shows that even in 20 min the particles cannot penetrate into the T-tubules of an intact cell (Fig. 3 *B*, *upper panel*) or the sarcoplasm of a permeabilized cell (Fig. 3 *B*, *lower panel*). The permeabilization of the cell was confirmed using the salt form of fluo-3 (Fig. 3 *C*). Unfortunately, this method did not allow the visualization of particles <50 nm in size. Thus, we used EM and silver enhancement to visualize smaller particles.

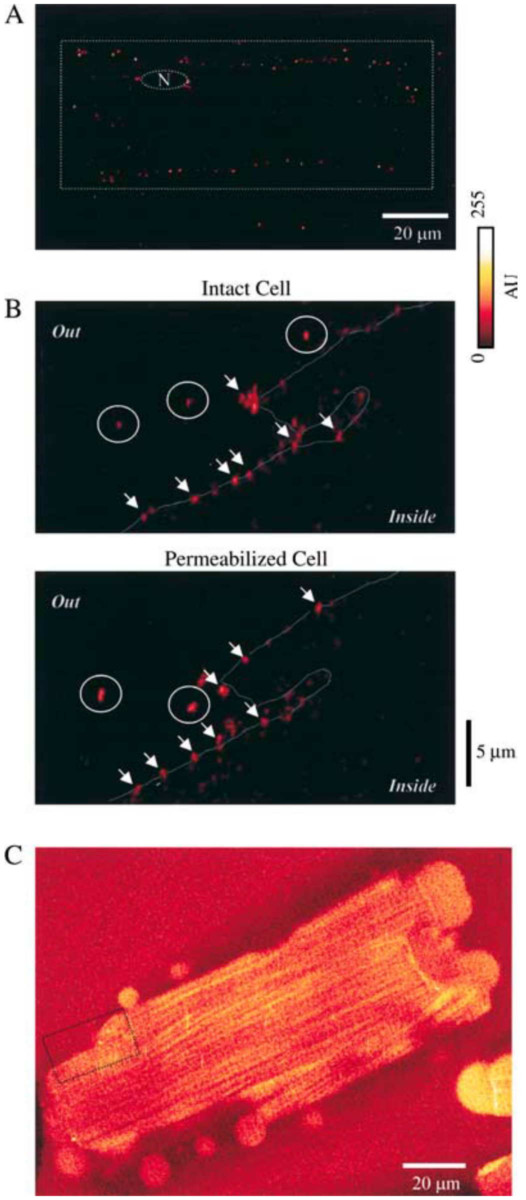

FIGURE 3 Confocal microscopy images showing the distribution of 51-nm particles in intact ventricular myocytes by means of reflected light. (*A* and *B*) PVP-coated 50-nm gold particles were added 5 min (*A*) or 20 min (*B*) before recording. (*A*) Representative image of a ventricular cell after digital contrasting. Dotted lines are drawn around the cell and nucleus (*N*). (*B*) Cell area (delineated by a box in *C*) before (*upper*) and after (*lower*) saponin permeabilization. The image after permeabilization was made 25 min after the addition of the second portion of 50-nm gold particles. Gold particles in the solution are marked with circles. Gold particles located presumably on the sarcolemma are marked with arrows. The sarcolemma is shown as a gray line. (*C*) The cell presented in *B* was loaded with 25 μM fluo-3 (pentapotassium salt) to demonstrate permeabilization. Excitation, 488 nm; emission, >505 nm; 100 nM Ca^{2+}.

Particles 3 nm in size were never found to be colocalized with any specific structure of the TATS and probably represent those particles which were uptaken into the sarcoplasm by endocytosis, whereas the rest were washed out of TATS during fixation (Fig. 4). The density of the particles was 0.34 ± 0.05 particles/μm^3 ($n = 215$) for quiescent cells (nominally Ca^{2+}-free Tyrode solution) and 0.11 ± 0.03 particles/μm^3 ($n = 162$) for contracting cells (5 mM Ca^{2+} in the Tyrode solution). Taking into account the 46% reduction in volume and the original density of the particles in the experimental solution (120 particles/μm^3), this means that only 1 of 512 particles entered a quiescent cell during 20 min of incubation. This ratio shows that 3-nm particles were mainly washed out of the TATS. Interestingly, the elevation of [Ca^{2+}] from 0 to 2 mM in the extracellular solution resulted in a significant increase in the density of particles in the cells (0.81 ± 0.07 particles/μm^3, $n = 152$, $P < 0.001$). However, these particles also were not colocalized with the TATS. Moreover, this density was also significantly higher

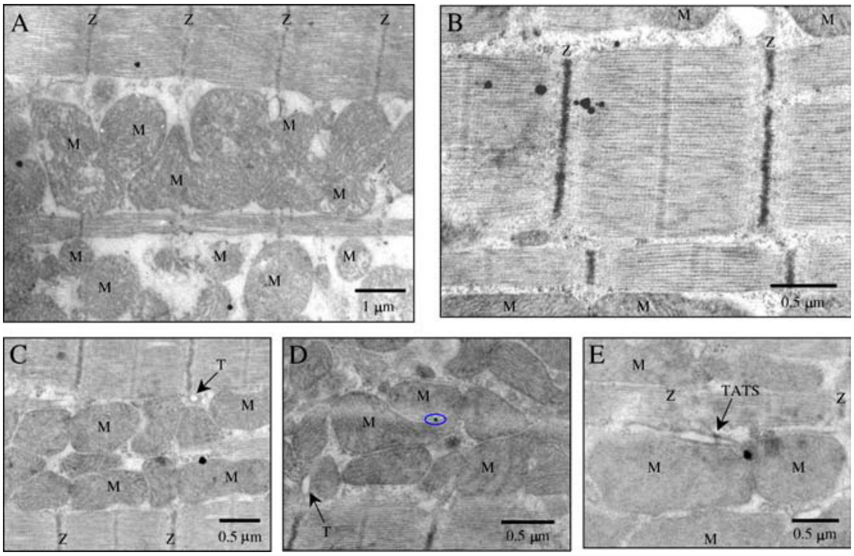

FIGURE 4 Representative electron micrographs made using fast conventional fixation and silver enhancement show the distribution of 3-nm particles in intact ventricular myocytes. *TATS*, transverse-axial tubular system; *T*, T-tubules; *M*, mitochondrion; *Z*, Z-line. The blue oval shows a nanoparticle located deeper inside the ultrathin section and therefore having a smaller diameter after silver enhancement.

than the density of the particles in 5 mM Ca^{2+}. This suggests that contraction plays a negative role in particle penetration into the TATS or the sarcoplasm.

In contrast to the distribution of the 3-nm particles, 6-nm particles were found primarily in TATS tubules (Fig. 5). Contracting cells contained ~2 times more 6-nm particles than quiescent ones. The presence of 5 mM of Ca^{2+} significantly increased the density of the particles inside the TATS in comparison to the nominally Ca^{2+}-free Tyrode solution (from 3.81 ± 0.78 particles/μm^3 to 8.95 ± 1.56 particles/μm^3, respectively; $n = 44$ and 32, respectively; $P < 0.01$). The elevation of [Ca^{2+}] from 0 to 2 mM in the

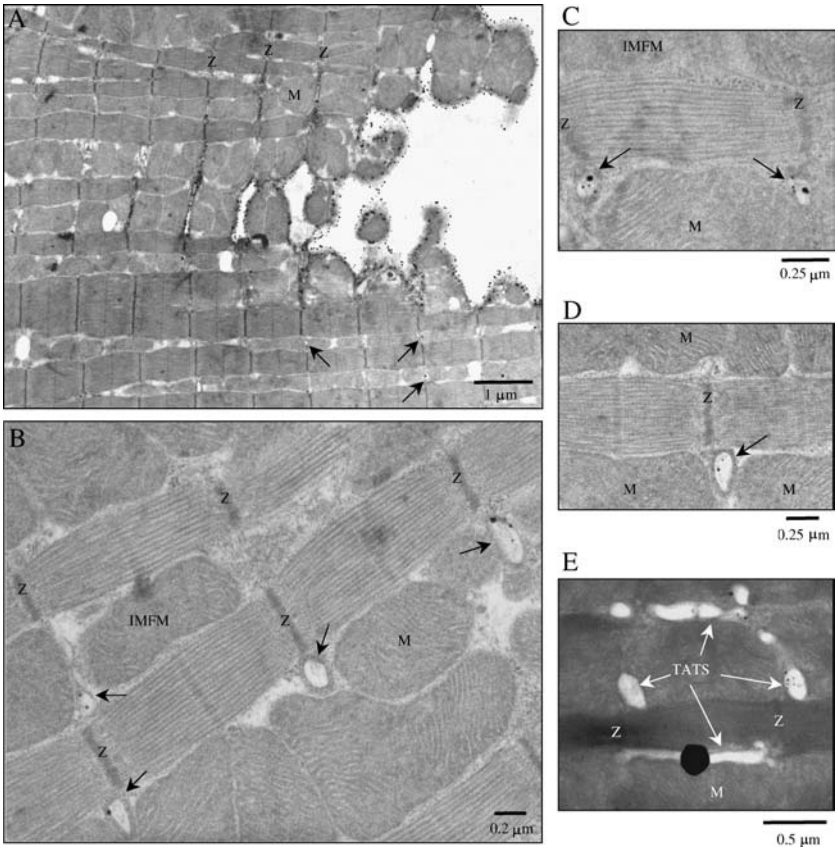

FIGURE 5 Electron micrographs made using fast conventional fixation and silver enhancement show the distribution of 6-nm particles in intact ventricular myocytes. Representative micrographs show the distribution of nanoparticles along the sarcolemma (*A*) and in the transverse-axial tubular system (*B*). Black arrows show T-tubules; *M*, mitochondrion; *IMFM*, intermyofibrillar mitochondrion; *Z*, Z-line.

extracellular solution did not change the particle density (3.15 ± 0.94 particles/μm^3; $n = 56$). Thus, unlike the 3-nm particles, the 6-nm particles were trapped mostly in the TATS. One of the possible mechanisms for the trapping is the binding to the oligosaccharide side chains of sarcolemmal glycoproteins. A slightly oblique section (Fig. 5 *A*) allows seeing how the sarcolemmal transversal invaginations covered with nanoparticles penetrate deeper and deeper into the cell until the beginning of the T-tubules, which are also filled with the particles. A similar surface structure of the ventricular cells was shown earlier in vivo using scanning ion conductance microscopy, and the transverse invaginations of the sarcolemma were named *z*-grooves (30).

We found 11-nm particles in the T-tubules of only the contracting cells, and the density of the particles was only 0.58 ± 0.16 particles/μm^3 ($n = 49$)(Fig. 6 *A*). The diffusion of the particles in the T-tubules could be decreased by the glycocalyx. This barrier could be partially destroyed by sialidase neuraminidase (1). Therefore, to check whether the glycocalyx was directly involved in the suppression of particle movement, we pretreated intact ventricular cells with 0.3 U/ml neuraminidase for 4 h in 5 mM Tyrode. The spontaneous contractions of Ca^{2+}-overloaded cells facilitated the wash-out of the destroyed parts of the TATS glycocalyx. This pretreatment made the transverse but not the longitudinal tubules of TATS more accessible for 11-nm particles, whereas particles $\geq$16 nm still could not enter it (Fig. 6, *B* and *C*). The graph presented in Fig. 6 *D* combines the density data for contracting ventricular cells before and after the neuraminidase treatment. Note that we did not find 16-nm particles inside the cells under control conditions.

Permeabilized ventricular myocytes

As we mentioned above, the confocal microscopy experiments showed that 51 nm particles could not enter saponin-permeabilized ventricular cells (Fig. 3 *B*). This could be directly related to the size of the membrane holes made with saponin under the conditions used. However, under our conditions saponin-permeabilized cells produced sarcolemmal bubbles from the stripped membrane (Fig. 3 *C*). During permeabilization only the outer part of the sarcolemma was damaged by saponin. The integrity of TATS was confirmed in our EM experiments with Epon embedding (not shown), whereas in experiments using mild LR White resin embedding we could not see the membranes clearly enough to make such conclusions.

After the incubation of ventricular cells with 0.01% saponin for 60 s (26), only 3- to 11-nm particles were found inside the cells. The nanoparticles were distributed unevenly: their density was higher closer to the sarcolemma. Also, smaller particles penetrated deeper into the cell and were distributed more evenly. The 3-nm particles were found practically everywhere (10 experiments), including in the nuclei and mitochondria, but not in the JC, IMFM-jSR, and intermitochondrial junctions (Fig. 7). Note that all particles are initially of equal size, and the size of the smaller particles on the micrographs resulted from a deeper location of gold

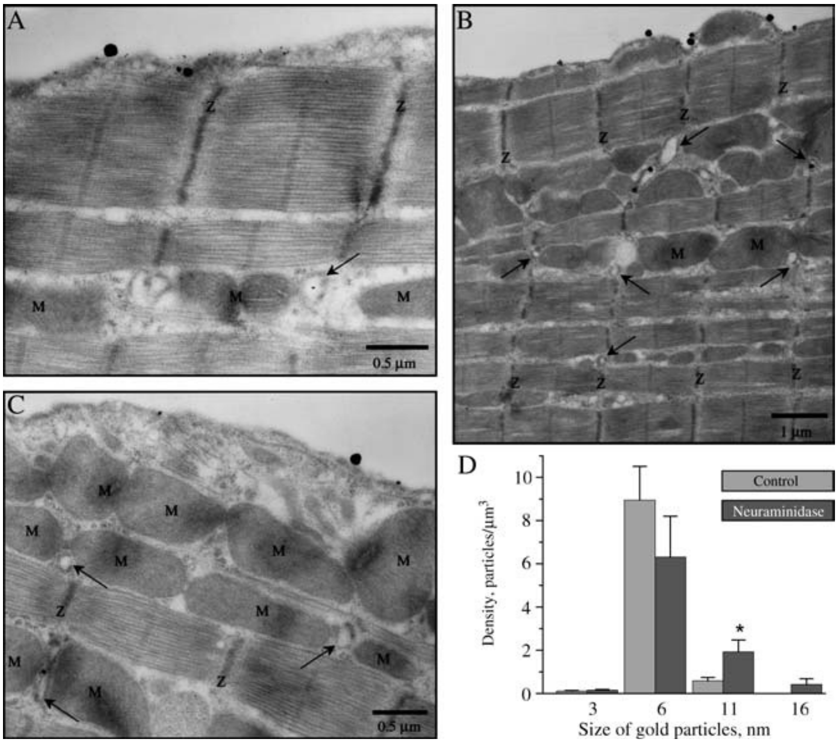

FIGURE 6 Distribution of 11-nm particles in contracting intact ventricular myocytes. (*A*–*C*) Electron micrographs made using fast conventional fixation and silver enhancement. Representative micrographs show the distribution of particles before (*A*, 11-nm particles) and after (*B*, 11-nm, and *C*, 16-nm particles) 4-h pretreatment with 0.3 U/ml neuraminidase. *M*, mitochondrion; *Z*, Z-line. T-tubules are marked by arrows. (*D*) Graphs representing the density of 3- to 16-nm particles in spontaneously contracting intact ventricular cells before (*gray*) and after (*dark gray*) 4 h of pretreatment with 0.3 U/ml neuraminidase ($n = 23$–190). An asterisk indicates data that are statistically different from the corresponding control ($P < 0.01$). $[Ca^{2+}] = 5$ mM.

particles in the ultrathin section and their relative inaccessibility for silver enhancement. Such particles can be seen well with a higher resolution. We marked them on our micrographs with blue ovals. The density of the particles was 4.03 ± 0.21 particles/μm^3 for quiescent cells ($n = 189$), and 2.16 ± 0.15 particles/μm^3 for contracting cells ($n = 287$). The density of the particles in the nucleus was not significantly different for quiescent and contracting cells (0.18 ± 0.06 and 0.09 ± 0.03 particles/μm^3, respectively, $n = 10$ each).

Although penetration of gold nanoparticles into the nucleus was shown earlier by other investigators (18,20–22), the penetration of these particles into mitochondria is shown here for the first time, to our knowledge. The particles were found primarily in the mitochondrial intermembrane space. However, the relative ''transparency'' of ultrathin sections under our conditions makes the results questionable. The particles could enter the mitochondrial intermembrane space only through the voltage-dependent anion channel (VDAC) (31,32). To clarify the localization of 3-nm particles we inhibited VDAC by 4,4-diisothiocyanatostilbene-2,2′-disulfonic acid (DIDS), König Polyanion (gift from Dr. Marco Colombini), or anti-Porin (Ab-5; Calbiochem, San Diego, CA). Preincubation of the cells for 30 min with 300 μM DIDS reduced the density of the nanoparticles in contracting cells by $\sim$80% (to 0.45 ± 0.11 particles/μm^3, $n = 33$), with 50 μg/ml König Polyanion by $\sim$85% (to 0.31 ± 0.10 particles/μm^3, $n = 52$), and with 5 μl anti-Porin by $\sim$80% (to 0.43 ± 0.08 particles/μm^3, $n = 88$). The effect of anti-Porin could be at least partly explained by its size (IgG, 150 kDa, $\sim$10 nm) (33). The antibodies could dramatically decrease diffusion of 3-nm particles into the sarcoplasm.

Fig. 8 shows representative micrographs of the contracting ventricular cells filled with 6-nm particles (4.89 ± 0.56 particles/μm^3, $n = 308$). We found them to be widely distributed in the sarcoplasm primarily within the I-bands near Z-lines (47 ± 4%, from 33 micrographs) even in the middle of cell (Fig. 8 *A*, *B*, and *D*). However, the particles were not found in the nuclei ($n = 37$), mitochondria, TATS, JC, IMFM-jSR, or intermitochondrial junctions (Fig. 8, *A* and *B*). Fig. 8 *C* shows that although some particles are located in close vicinity to the nucleus, neither one has entered it. A similar distribution of the nanoparticles was recorded in nine other nuclei. An increase of [Ca^{2+}] up to 400 nM (not shown) did not change the distribution of the 6-nm particles.

Nanoparticles with diameter 11 nm were found only in close vicinity to the sarcolemma (Fig. 9 *A*) and in the same density for contracting or quiescent cells (0.46 ± 0.12 particles/μm^3 and 0.43 ± 0.16 particles/μm^3, respectively, $n = 38$ for each). The entering of the particles into the sarcoplasm could be suppressed in our experiments by the cytoskeleton (1). The cytoskeletal barrier can be partially destroyed by the potent inhibitor of actin polymerization,

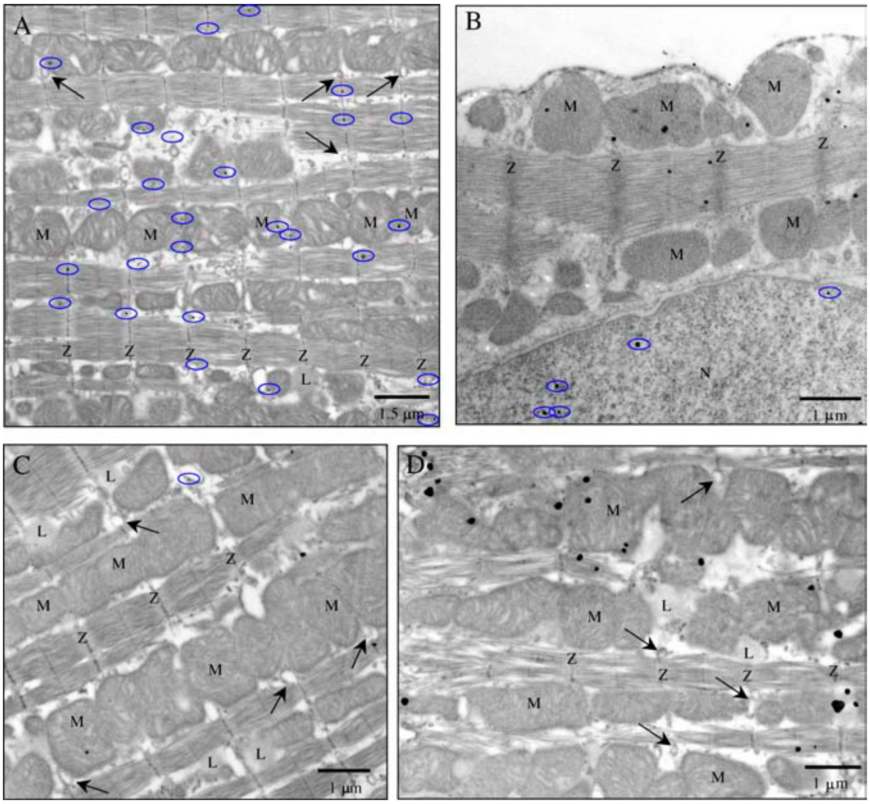

FIGURE 7 Electron micrographs made using fast conventional fixation and silver enhancement show the distribution of 3-nm particles in permeabilized ventricular myocytes. Representative micrographs show that after partial wash-out during fixation, some nanoparticles are still trapped inside the myocyte in the sarcoplasm, in the nucleus (*B*), near mitochondria, and inside mitochondria. *M*, mitochondrion; *Z*, Z-line; *N*, nucleus; *L*, lipid droplet. Arrows indicate T-tubules and blue ovals show nanoparticles located deeper inside the ultrathin section, which therefore have a smaller diameter after silver enhancement.

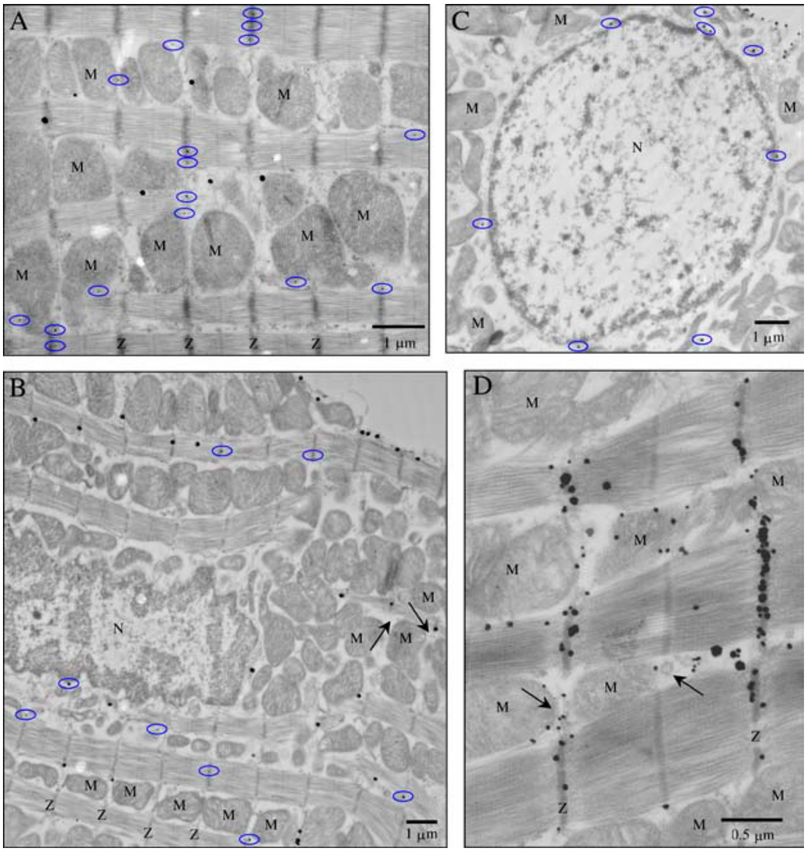

FIGURE 8 Distribution of 6-nm particles in permeabilized ventricular myocytes. Representative electron micrographs made using fast conventional fixation and silver enhancement show the distribution of nanoparticles in the cytoplasm, but not in the nucleus (*B* and *C*) or mitochondria. *M*, mitochondrion; *Z*, Z-line; *N*, nucleus. Arrows indicate T-tubules and blue ovals show nanoparticles located deeper inside the ultrathin section, which therefore have smaller diameters after silver enhancement.

cytochalasin D. Therefore, to check whether the particle entering was restricted by the cytoskeleton, we pretreated contracting permeabilized ventricular cells with 40 μM cytochalasin D for 20 min. Spontaneous contraction facilitated the disruption of the cytoskeleton. After this pretreatment, 11-nm particles were found in the sarcoplasm (Fig. 9, *B* and *C*), but not in the mitochondria or the nucleus. The particles were located primarily within the I-bands (64 ± 6% of 10-nm particles, from 15 micrographs). Particles with diameter $\geq$16 nm could not enter the cells even after the treatment with cytochalasin D. The graph presented in Fig. 9 *D* combines the density data for contracting ventricular cells before (*gray*) and after the treatment with cytochalasin D (the latter is presented only for particles that could not easily penetrate into the sarcoplasm under the control conditions).

DISCUSSION

The normal functioning of a cardiac cell is very dependent on the aqueous diffusion of ions and macromolecules in the sarcoplasm. Intuitively, the inhibition of the pathways due to damage of the cytoskeleton or overexpression of proteins could result in problems with 1), the delivery of macromolecules (such as RNAs and structural and regulatory proteins) and 2), the degradation of aged proteins. The aqueous pathways inside a ventricular cell could be divided into two groups: 1), the extracellular tubules of the TATS; and 2), the sarcoplasmic pathways. Unfortunately, electron microscopy could not be used directly for their measurements due to the multiple effects of fixatives, contrasting agents, and preparation procedures on cell volume, intracellular structures, and their appearance on a micrograph. The ''most effective'' stages of the preparation for reducing cell volume are dehydration and resin polymerization (8) (Table 1).

We investigated for the first time what we know of the real accessibility of TATS and sarcoplasmic aqueous diffusion pathways. The latter is a most delicate intracellular ''structure'' that has not been seen on micrographs even with the highest resolution, despite its taking up ~50% of the cell volume before fixation and the embedding of the cell for EM.

Methodology

Although particles of only one size were used for each experiment, silver grains of different sizes could be found after silver enhancement. The buildup of silver on the particles is a time-dependent process and could be restricted by local conditions. The small size of some particles, as well as the incorrect shape of silver granules (the standard shape for silver grains grown on PVP-coated gold is a triangle with cut corners; see Fig. 4, *A* and *B*), can be explained by the penetration of $AgNO_3$ into the inside of the ultrathin section facilitated by the water-soluble LR White resin used for

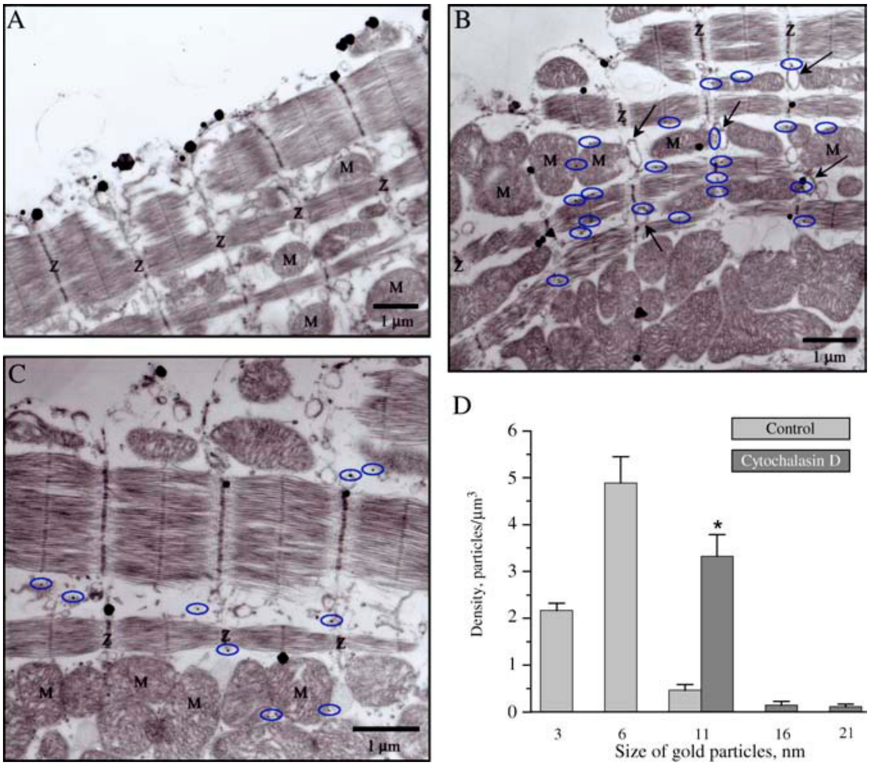

FIGURE 9 (*A–C*) Electron micrographs made using fast conventional fixation and silver enhancement show the distribution of 11-nm particles in permeabilized ventricular myocytes. Representative micrographs show the distribution of the nanoparticles before (*A*) and after (*B* and *C*) partial ablation of the cytoskeleton (20 min pretreatment with 40 μM cytochalasin D). (*D*) Graphs representing the density of nanoparticles (3–21 nm) in intact ventricular cells before (*gray*) and after (*dark gray*, only for particles $\geq$11 nm) 20 min of pretreatment with 40 μM cytochalasin D ($n = 26$–308). Asterisks indicate data that are statistically different from the corresponding control ($P <$ 0.001). *M*, mitochondrion; *Z*, Z line. Arrows indicate T-tubules and blue ovals show nanoparticles located deeper inside the ultrathin section, which therefore have smaller diameters after silver enhancement.

embedding. This penetration should be similar to that shown for uranyl acetate and lead citrate (34–36). Thus, every ultrathin section has to be contrasted throughout the entire thickness (but the closer to the surface of application, the stronger), and the size of silver grain shows how far from the surface of the section the nanoparticles were originally located. To maximally preserve the tissue and sarcoplasm we used very fast fixation and ''soft'' embedding. The best conditions were found in preliminary EM experiments varying the time of fixation as well as the concentrations and proportions of fixatives.

Transverse-axial tubular system

Our experiments showed the importance of the intratubular glycocalyx in preventing big particles from infiltrating into the TATS. Earlier, the diameter of T-tubules was evaluated mainly from EM micrographs. It was found to be ~300 nm, whereas sometimes the diameters of TATS elements could be as small as 40 nm (10). We found that only particles ~6 nm in size could penetrate the TATS (Fig. 6 *D*). This penetration was significantly facilitated with 5 mM Ca^{2+} and/or corresponding cell contraction. Surprisingly, 3-nm and sometimes 6-nm particles added to intact ventricular cells were found inside the cell (Fig. 4), including in the mitochondria and nucleus. Because TATS tubules were not shown to penetrate into the mitochondria or the nucleus, we suggest that the 3-nm particles added to intact cells entered the cytoplasm by endocytosis. Unfortunately, the special conditions of cell fixation and resin polymerization, and also a partial reduction of image quality with silver enhancement, did not allow us to visualize membranes of the endocytotic vesicles, and thus we cannot confirm this hypothesis. However, despite the uncertainty in the actual mechanisms of penetration of the nanoparticles into the sarcoplasm, we can conclude that the penetration was inhibited by contractile activity or low $[Ca^{2+}]$. Indeed, the density of 3-nm particles was significantly lower in nominally Ca^{2+}-free Tyrode solution than in the solution containing 2 mM Ca^{2+}. An additional increase of $[Ca^{2+}]$ to 5 mM induced spontaneous Ca^{2+} waves and significantly decreased the density of the nanoparticles. This could result from the inhibition of 5 mM Ca^{2+} on the movement of 3-nm particles in the TATS or through the sarcolemma. However, 5 mM Ca^{2+} facilitated the penetration of larger, 6-nm particles into TATS. Thus, contractility was the mechanism that mediated the inhibitory effect of 5 mM Ca^{2+} on the penetration of the smaller 3-nm particles through the sarcolemma of the intact cells. At least partially, this effect of contractility could be explained by the movement of TATS sarcolemma during a contraction.

Sarcoplasm

To allow nanoparticles to penetrate the sarcoplasm, we permeabilized the sarcolemma with saponin. Fig. 3 *C* shows that a typical saponin-permeabilized cell produced sarcolemmal bubbles. The number and diameter of the bubbles showed that the sarcoplasm was opened for penetration by nanoparticles and only its viscosity and cytoskeleton could restrict the penetration. The lack of particles in the TATS suggests that the permeabilization probably mechanically restricted the entrance of nanoparticles to the TATS by sealing the T-tubules.

We found that particles were distributed unevenly in the sarcoplasm. Particles $\geq$6 nm were localized primarily within the I-bands (37) near the Z-lines. For example, Fig. 8, *A* and *B*, shows that ~60% of the particles are located within the I-bands, whereas they take up $\ll$10% of the sarcomere. At higher magnification (Fig. 8 *D*), it is clearly seen that silver grains are located on less electron-dense (lighter) areas of the I-band (two lines of particles along both sides of the Z-line).

Because the density of the particles that entered the sarcoplasm was greater closer to the outer sarcolemma, we suggest that 6-nm particles could move faster along the I-bands (i.e., transversally) and that they had a significant delay in the exits to the longitudinal pathways. It is important that 3-nm particles did not show this delay. Thus, the diffusion velocity of the 6-nm particles was restricted by some intracellular structures. Therefore, we suggest that the distribution of 6-nm particles shows the existence in ventricular cells of at least two aqueous traffic pathways for nanoparticles with diameter $\geq$6 nm: slow and fast. The former pathways are longitudinal narrow intermyofibrillar ''streets'' available primarily for the fast diffusion of particles <6 nm in diameter; and the later paths are wide ''avenues'' across a myofibril (around Z-lines) for fast diffusion of particles with size $\geq$6 nm and up to 11 nm. Taking into account the gyration diameters for proteins (15), the diffusion of proteins $\geq$60 kDa should be significantly inhibited in the longitudinal direction. This may explain discrepancies between immunofluorescent and immunogold labeling. The former approach uses permeabilization for the delivery of the antibodies into the cell. In this case, there is a possibility that the huge antibodies (IgG, ~150 kDa, ~10 nm in diameter) will be located primarily along the Z-lines and that immunogold labeling will not confirm this distribution, as was shown by Larsen et al. (38) for ribosome distribution in a rat heart. Based on our data presented here we would recommend using Fab fragments of primary IgG conjugated with a fluorescent probe for immunofluorescent labeling. However, in the case of using big (i.e., Quantum Dots, up to 10 nm; Quantum Dot Corporation, Hayward, CA) or uncalibrated fluorescent markers, similar problems can arise from restrictions in their diffusion inside the cell.

The restriction of the JC for particles >3 nm confirms the recently published data about colocalization of RyRs (39). Initially we suggested the existence of physical contacts between RyRs based on studies from the Marks laboratory (40) and on the analysis of our micrographs similar to the one presented in Fig. 1 *C*. Such regularity in the distribution of RyRs could not be seen very often and is unique even for the same slice. This supposes a role for the angle of section in the cell and, assuming penetration of contrasting agents, for slice thickness in viewing the distribution. RyR is a protein with side length of ~27 nm (41), and an ultrathin section is ~80 nm deep. Thus, we could see RyRs as electron-dense structures only if they are distributed in a checkered order in the membrane of the jSR and the section is perpendicular to the T-tubule. However, even in this case, visualized contacts between proteins, as well as contacts between mitochondria and jSR, and intermitochondrial contacts (Fig. 1 *D*), could be artifacts resulting form the preparation of the cell for EM. Our experiments confirmed that the zones were originally restricted for particles >3 nm. At the same time, VDAC allows particles up to 3 nm in size to pass through it, being a much wider gate to the mitochondrial gaps than the entrances from the sarcoplasmic site. Thus, we can suggest the existence of pathways for direct delivery of mitochondrial products to the jSR and that mitochondria share these products and products involved in mitochondrial metabolism. The existence of such pathways was predicted earlier by Bakeeva et al. (42).

Our data also showed that the delivery and removal of big proteins to all of the three gaps between mitochondria, jSR, and T-tubules could occur only through lateral membrane diffusion. For example, RyRs (approximate dimensions 27 × 27 × 23 nm) (41) could move into or out of the JC only using the mechanism of lateral diffusion in the SR membrane. Moreover, the construction of macromolecular complexes regulating cardiac RyR function (2) suggests preconstruction and lateral diffusion of functional groups to the JC. Our preliminary data confirmed the existence of such groups (43). Ultrastructurally, they are probably seen on micrographs as a corbular SR (44), the function of which as yet remains unknown.

Mitochondria voltage-dependent anion channel (VDAC)

Our data showed the presence of some silver particles inside mitochondria. Located in the outer mitochondrial membrane, VDAC is the only way for nanoparticles to get inside undamaged mitochondria. The physical size of the VDAC was suggested to be ~3 nm (45–47), and our EM experiments with permeabilized cells (Epon embedding, not shown) demonstrated the structural integrity of the mitochondria and their outer membranes in permeabilized ventricular cells. Thus, the data presented showed that VDAC's physical size is $\geq$3 nm but <6 nm. Our experiments with VDAC inhibitors, DIDS and König Polyanion (48–50), confirmed this conclusion. Although we used a monoclonal antibody against an outer part of the VDAC (for a sequence located on the edge of the channel pore), the reduction of nanoparticle density inside the mitochondria by the monoclonal antibody to VDAC could also be explained by a relative restriction of nanoparticle entry into the sarcoplasm by the huge IgG molecules. Unfortunately, sometimes mitochondrial granules (37,51) that are easily seen with Epon embedding

(Fig. 1 *A*) could also be present on LR White micrographs (one of them can be seen in Fig. 8 *B*; bottom part of the image). However, these granules are very rare and are not as electrondense as silver grains. Therefore, we could recognize them by digitally reducing the contrast of the micrograph. Also, on some images (not shown) the silver grains had a shape typical for PVP-coated sols.

Nucleus

The nuclear pore complex (NPC) is the most likely path for diffusion of the nanoparticles into the nucleus. For nonmuscle tissues, NPC was shown to be penetrable for particles $\leq$14 nm (21). Contrary to this, our experiments showed that NPC in ventricular cells could be penetrated only by particles with diameter $<$6 nm. This could be explained by low $[Ca^{2+}]$ (52); however, Ca^{2+} waves, as well as a permanent increase in $[Ca^{2+}]$ (up to 400 nM), kept 6-nm particles from penetrating into the nucleus. We suggest that the penetration of gold particles $>$6 nm into the nucleus, described earlier, was facilitated by the method of their delivery to the cytoplasm (microinjection), causing some damage to the cytoskeleton.

The presented data allow us to conclude that, in rat ventricular cells 1), the TATS and the sarcoplasm are accessible only for particles $\leq$11 nm; 2), the gaps between T-tubules and jSR, jSR and mitochondria, and intermitochondrial contacts are inaccessible for particles with physical size $\geq$3 nm; 3), the VDAC and NPR could not be penetrated with particles $\geq$6 nm; and 4), there is a difference in size clearance between transversal (along Z-lines) and longitudinal (along myofibrils) sarcoplasmic aqueous diffusional pathways.

This work was supported by grants from the National Institutes of Health (HL36974, HL70709, HL67849, and HL25675).

REFERENCES

1. Bers, D. M. 2001. Excitation-contraction coupling and cardiac contractile force. Kluwer Academic Publishers, Dordrecht, The Netherlands.
2. Bers, D. M. 2004. Macromolecular complexes regulating cardiac ryanodine receptor function. *J. Mol. Cell. Cardiol.* 37:417–429.
3. Berridge, M. J., M. D. Bootman, and H. L. Roderick. 2003. Calcium signalling: dynamics, homeostasis and remodelling. *Nat. Rev. Mol. Cell Biol.* 4:517–529.
4. Wehrens, X. H., S. E. Lehnart, and A. R. Marks. 2005. Intracellular calcium release and cardiac disease. *Annu. Rev. Physiol.* 67:69–98.
5. Sommer, J. R., and E. A. Johnson. 1968. Cardiac muscle. A comparative study of Purkinje fibers and ventricular fibers. *J. Cell Biol.* 36:497–526.
6. Frank, J. S. 1990. Ultrastructure of the unfixed myocardial sarcolemma and cell surface. *In* Calcium and the Heart. G. A. Langer, editor. Raven Press, New York. 1–25.
7. Flucher, B. E., and C. Franzini-Armstrong. 1996. Formation of junctions involved in excitation-contraction coupling in skeletal and cardiac muscle. *Proc. Natl. Acad. Sci. USA.* 93:8101–8106.
8. Eisenberg, B. R., and B. A. Mobley. 1975. Size changes in single muscle fibers during fixation and embedding. *Tissue Cell.* 7:383–387.
9. Pease, D. C., and K. R. Porter. 1981. Electron microscopy and ultramicrotomy. *J. Cell Biol.* 91:287s–292s.
10. Forbes, M. S., and E. E. van Neil. 1988. Membrane systems of guinea pig myocardium: ultrastructure and morphometric studies. *Anat. Rec.* 222:362–379.
11. Ogata, T., and Y. Yamasaki. 1993. Ultra-high resolution scanning electron microscopic studies on the sarcoplasmic reticulum and mitochondria in various muscles: a review. *Scanning Microsc.* 7: 145–156.
12. Soeller, C., and M. B. Cannell. 1999. Examination of the transverse tubular system in living cardiac rat myocytes by 2-photon microscopy and digital image-processing techniques. *Circ. Res.* 84: 266–275.
13. Marcus, Y. 1994. A simple empirical model describing the thermodynamics of hydration of ions of widely varying charges, sizes, and shapes. *Biophys. Chem.* 51:111–127.
14. Gittins, D. I., and F. Caruso. 2002. Biological and physical applications of water-based metal nanoparticles synthesized in organic solution. *ChemPhysChem.* 3:110–113.
15. Vandegriff, K. D., M. McCarthy, R. J. Rohlfs, and R. M. Winslow. 1997. Colloid osmotic properties of modified hemoglobins: chemically cross-linked versus polyethylene glycol surface-conjugated. *Biophys. Chem.* 69:23–30.
16. Merzlyak, P. G., L. N. Yuldasheva, C. G. Rodrigues, C. M. Carneiro, O. V. Krasilnikov, and S. M. Bezrukov. 1999. Polymeric nonelectrolytes to probe pore geometry: application to the alpha-toxin transmembrane channel. *Biophys. J.* 77:3023–3033.
17. De Roe, C., P. J. Courtoy, and P. Baudhuin. 1987. A model of protein-colloidal gold interactions. *J. Histochem. Cytochem.* 35:1191–1198.
18. Feldherr, C. M. 1965. The effect of the electron-opaque pore material on exchanges through the nuclear annuli. *J. Cell Biol.* 25:43–53.
19. Pastoriza-Santos, I., and L. M. Liz-Marzan. 2002. Formation of PVP-protected metal nanoparticles in DMF. *Langmuir.* 18:2888–2894.
20. Dworetzky, S. I., and C. M. Feldherr. 1988. Translocation of RNA-coated gold particles through the nuclear pores of oocytes. *J. Cell Biol.* 106:575–584.
21. Feldherr, C. M., and D. Akin. 1990. EM visualization of nucleocytoplasmic transport processes. *Electron Microsc. Rev.* 3:73–86.
22. Feldherr, C. M., D. Akin, and R. J. Cohen. 2001. Regulation of functional nuclear pore size in fibroblasts. *J. Cell Sci.* 114:4621–4627.
23. DuBell, W. H., W. J. Lederer, and T. B. Rogers. 2000. K^+ currents responsible for repolarization in mouse ventricle and their modulation by FK-506 and rapamycin. *Am. J. Physiol. Heart Circ. Physiol.* 278: H886–H897.
24. Lukyanenko, V., S. Subramanian, I. Györke, T. Wiesner, and S. Györke. 1999. The role of sarcoplasmic reticulum luminal Ca^{2+} in generation of Ca^{2+} wave in rat ventricular myocytes. *J. Physiol.* 518: 173–186.
25. Lukyanenko, V., S. Viatchenko-Karpinski, A. Smirnov, T. F. Wiesner, and S. Györke. 2001. Dynamic regulation of the SR Ca^{2+} content by lumenal Ca^{2+}-sensitive leak through RyRs in rat ventricular myocytes. *Biophys. J.* 81:785–798.
26. Lukyanenko, V., and S. Györke. 1999. Ca^{2+} sparks and Ca^{2+} waves in saponin-permeabilized cardiac myocytes. *J. Physiol.* 521:575–585.
27. Sun, Y., and Y. Xia. 2002. Shape-controlled synthesis of gold and silver nanoparticles. *Science.* 298:2176–2179.
28. Thomas, K. G., and P. V. Kamat. 2000. Making gold nanoparticles glow: Enhanced emission from a surface-bound fluoroprobe. *J. Am. Chem. Soc.* 122:2655–2656.
29. De Brabander, M., G. Geuens, R. Nuydens, M. Moeremans, and J. De Mey. 1985. Probing microtubule-dependent intracellular motility with nanometre particle video ultramicroscopy (nanovid ultramicroscopy). *Cytobios.* 43:273–283.

30. Korchev, Y. E., Y. A. Negulyaev, C. R. Edwards, I. Vodyanoy, and M. J. Lab. 2000. Functional localization of single active ion channels on the surface of a living cell. *Nat. Cell Biol.* 2:616–619.
31. Colombini, M. 1987. Regulation of the mitochondrial outer membrane channel, VDAC. *J. Bioenerg. Biomembr.* 19:309–320.
32. Mannella, C. A. 1998. Conformational changes in the mitochondrial channel protein, VDAC, and their functional implications. *J. Struct. Biol.* 121:207–218.
33. Feldkamp, C. S., and J. L. Carey. 1996. Immune function and antibody structure. *In* Immunoassay. E. P. Diamandis and T. K. Christopoulos, editors. Academic Press, New York. 5–24.
34. Shalla, T. A., T. W. Carroll, and G. A. Dezoeten. 1964. Penetration of stain in ultrathin sections of tobacco mosaic virus. *Stain Technol.* 39: 257–265.
35. Chan-Curtis, V., W. D. Belt, and C. T. Ladoulis. 1970. Cytochemical localization of nucleic acids by an acriflavine-phosphotungstate complex for fluorescence microscopy and electron microscopy. *J. Histochem. Cytochem.* 18:609–627.
36. Peters, A., P. L. Hinds, and J. E. Vaughn. 1971. Extent of stain penetration in sections prepared for electron microscopy. *J. Ultrastruct. Res.* 36:37–45.
37. Fawcett, D. W., and N. S. McNutt. 1969. The ultrastructure of the cat myocardium. I. Ventricular papillary muscle. *J. Cell Biol.* 42:1–45.
38. Larsen, T. H., J. E. Hesketh, S. Rotevatn, G. Greve, and T. Saetersdal. 1994. Ribosome distribution in normal and infarcted rat hearts. *Histochem. J.* 26:79–89.
39. Yin, C. C., L. M. Blayney, and F. Anthony Lai. 2005. Physical coupling between ryanodine receptor-calcium release channels. *J. Mol. Biol.* 349:538–546.
40. Marx, S. O., J. Gaburjakova, M. Gaburjakova, C. Henrikson, K. Ondrias, and A. R. Marks. 2001. Coupled gating between cardiac calcium release channels (ryanodine receptors). *Circ. Res.* 88:1151–1158.
41. Fleischer, S., and M. Inui. 1989. Biochemistry and biophysics of excitation-contraction coupling. *Annu. Rev. Biophys. Biophys. Chem.* 18:333–364.
42. Bakeeva, L. E., Y. S. Chentsov, and V. P. Skulachev. 1983. Intermitochondrial contacts in myocardiocytes. *J. Mol. Cell. Cardiol.* 15:413–420.
43. Salnikov, V. V., A. Lukyanenko, W. J. Lederer, and V. Lukyanenko. 2005. Spatial distribution of ryanodine receptors in rat ventricular cells. *Biophys. J.* 88:87a (Abstr.)
44. Dolber, P. C., and J. R. Sommer. 1984. Corbular sarcoplasmic reticulum of rabbit cardiac muscle. *J. Ultrastruct. Res.* 87:190–196.
45. Mannella, C. A. 1987. Electron microscopy and image analysis of the mitochondrial outer membrane channel, VDAC. *J. Bioenerg. Biomembr.* 19:329–340.
46. Mannella, C. A. 1992. The 'ins' and 'outs' of mitochondrial membrane channels. *Trends Biochem. Sci.* 17:315–320.
47. Carneiro, C. M. M., P. G. Merzlyak, L. N. Yuldasheva, L. G. Silva, F. P. Thinnes, and O. V. Krasilnikov. 2003. Probing the volume changes during voltage gating of Porin 31BM channel with nonelectrolyte polymers. *Biochim. Biophys. Acta.* 1612:144–153.
48. König, T., B. Kocsis, L. Meszaros, K. Nahm, S. Zoltan, and I. Horvath. 1977. Interaction of a synthetic polyanion with rat liver mitochondria. *Biochim. Biophys. Acta.* 462:380–389.
49. Colombini, M., C. L. Yeung, J. Tung, and T. König. 1987. The mitochondrial outer membrane channel, VDAC, is regulated by a synthetic polyanion. *Biochim. Biophys. Acta.* 905:279–286.
50. Thinnes, F. P., H. Florke, H. Winkelbach, U. Stadtmuller, M. Heiden, A. Karabinos, D. Hesse, H. D. Kratzin, E. Fleer, and N. Hilschmann. 1994. Channel active mammalian porin, purified from crude membrane fractions of human B lymphocytes or bovine skeletal muscle, reversibly binds the stilbene-disulfonate group of the chloride channel blocker DIDS. *Biol. Chem.* 375:315–322.
51. Peachey, L. D. 1964. Electron microscopic observations on the accumulation of divalent cations in intramitochondrial granules. *J. Cell Biol.* 20:95–111.
52. Perez-Terzic, C., A. M. Gacy, R. Bortolon, P. P. Dzeja, M. Puceat, M. Jaconi, F. G. Prendergast, and A. Terzic. 1999. Structural plasticity of the cardiac nuclear pore complex in response to regulators of nuclear import. *Circ. Res.* 84:1292–1301.